Hidden defect identification in carbon fibre reinforced polymer plates using magnetic induction tomography

Lu Ma and Manuchehr Soleimani

Engineering Tomography Laboratory (ETL), Department of Electronic and Electrical Engineering, University of Bath, Bath, UK

E-mail: l.ma2@bath.ac.uk and m.soleimani@bath.ac.uk

Abstract. Carbon fibre reinforced polymer (CFRP) materials pose new challenges to the non-destructive evaluation (NDE) techniques. This study addresses the issue of large defect identification in CFRP plates using electromagnetic measurements. A dual plane magnetic induction tomography (MIT) technique is proposed as a method for damage localisation in composite parts, where two arrays of planar sensors are utilised to measure the changes in induced voltages due to the changes in electrical conductivity properties. This geometry meets the requirements of damage inspection in plate structures and thus makes the imaging process feasible. The electrical voltage measurements are used as input to inversely map the spatial resolution of the samples in the region of interest. The stability and detectability of the dual plane system is examined using small metallic cubes. Both individual and multiple instances of damage embedded in CFRP samples are created as a representation of possible manufacturing defects. Experimental study shows that the presence of damage can be identified in both cases using dual plane MIT system. With advanced sensing design, rapid data collection unit and improvement in resolution, MIT could become a rapid NDE technique for the integrity inspection of the composite structures.

Keywords: magnetic induction tomography, carbon fibre reinforcement polymer, dual-plane sensor array, non-destructive evaluation

Introduction

A new breed of high strength material, CFRP, has found widespread application in commercial aircraft, industrial and transportation markets, where strength, stiffness, a lower weight, and outstanding fatigue characteristics are crucial requirements. Structural health monitoring (SHM) of the CFRP such as missing carbon-fibre bundles, lanes, suspensions, fringes, missing sewing threads, angle errors and hidden manufacturing defects is an invaluable quality control. Many non-destructive evaluation (NDE) techniques have been applied in this area to CFRP, including low frequency vibration [1], ultrasonic methods [2, 3, 4, 5], radiography [6, 7, 8], thermography [9, 10] and eddy current testing [11, 12, 13, 14]. More recently, soft field tomography techniques have also been used for damage detection in CFRP using electrical impedance tomography (EIT) [15, 16, 17]; however, the MIT-based research in this area remains very limited [18].

Although the resolution of MIT is relatively low compared to X-ray tomography, the implementation of this technique benefits from its contact-less nature. There is no requirements for close contact such as gels (various ultrasonic methods), specially designed probes (eddy current testing and injected current thermography) or electrodes attached to the composites parts (EIT). As the carbon fibres in CFRP exhibit electrical conductivity, MIT could be a potential NDE technique providing a tomographic approach to traditional eddy current testing. MIT uses inductive coils to measure the induced voltages, which are associated with the passive electromagnetic properties non-linearly. The fundamental physics of MIT derive from the mutual inductance and eddy current theories. By passing an alternating current into an exciting coil, the sensing coil experiences a time-varying magnetic field. If materials with electrical properties are presented between this coil pair, the eddy currents arise in the conducting region, resulting in a perturbation in the magnetic field, that can be sensed by the receiving coil. As such, the electrical properties can be revealed, and the characteristics of the material presented in a reconstructed image, where the quality can be assessed visually. This technique has been applied in both biomedical and industrial processes [19, 20, 21, 22, 23, 24].

In this study, a dual plane MIT is proposed for the identification of large area hidden damage in CFRP. This dual plane sensor arrays realise the imaging process in 3D, providing informtion about the geometry of the testing samples. This geometry can be potentially used in the inspection of production line at the manufacturing stage. The system resolution is evaluated through both simulation and experiments. Results of the inspection of embedded defects in CFRP are presented. With advanced excitation and sensing topology [25], a fast data collection component and improved resolution, MIT could evolve to a rapid NDE technique for the structural health monitoring of CFRP.

Dual plane MIT system

The dual plane MIT system has been developed using two planar sensor arrays. The separation between the two arrays is $4cm$. Each array consists of 9 air-core cylindrical coils, which are arranged in a 3×3 matrix form. A non-conductive plate with a surface area of $14 \times 14cm^2$ is used to hold the sensors in place. Each coil has 100 turns, a side length of $3.4cm$, and the inner and outer diameters of the coils are $3.9cm$ and $4.1cm$ respectively (Figure 2a). The coil sequence of the first plane is shown in Figure 2b,

the second planar array follows the same numbering system.

The MIT measurement system block diagram is shown in Figure 1. In this study, a topward 8112 digital function generator is used to provide a signal of $15V$ peak at a driving frequency of $50KHz$. The choice of driving frequency depends on the the properties of the test materials and the skin depth required to penetrate such material. This will be discussed in section 4. An in-house printed circuit board (PCB) is designed to accomplish the channel switching process. The PCB consists of four $ADG406$ chips and one $SN74LS04N$ chip. The $ADG406$ is a monolithic $CMOS$ analog chip. It has several advantages including low power dissipation, high switching speed and low on resistance. The $SN74LS04N$ functions as a digital inverter, which is essential to switch the functions of the $ADG406$ chips between transmitting and receiving signals. The digital inverter requires a power supply of $5V$, supplied by the function generator. Each channel conducts equally well in both directions as long as the device is enabled and has an input signal range within the supply. All channels exhibit break-before-make switching action, preventing momentary shorting when switching channels. A $NI6295$ data acquisition device is connected through USB ports to interface between the PCB and a host PC, where the image reconstruction takes place. The $NI6295$ has four analog outputs at 16 bits and an input with a max rate of $1.25MS/s$. The aim of this device is to collect individual data efficiently, combine data effectively and display data in images to suit the need for imaging process. This process is controlled by LabView program. A description of the system hardware development has been reported in [24]. This system architecture has also been used for several MIT applications [26, 27, 28, 29, 30].

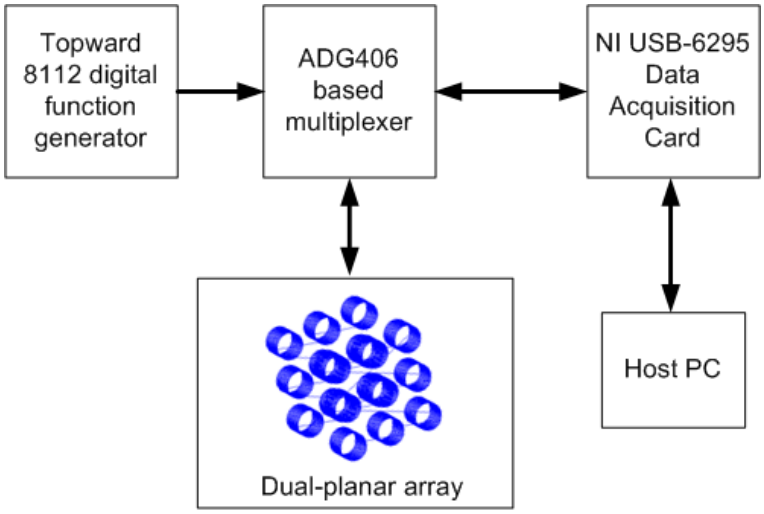

Figure 1. Block diagram of dual plane MIT system.

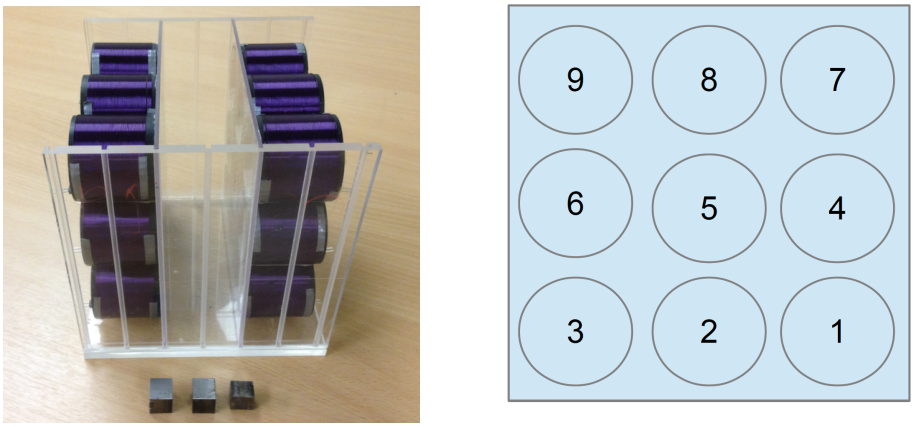

(a) (b)

Figure 2. (a) Dual plane sensor array; (b) Coil sequence of the first planar array.

Forward and inverse problems

In this study, a reduced magnetic vector potential is used to avoid modelling the structure of the coils using edge finite element method (FEM) [31, 32]. In the (A, A) formulation we have:

$$\nabla \times (\frac{1}{\mu}\nabla \times A_r) + j\omega\sigma A_r = \nabla \times H_s - j\omega\sigma A_s - \nabla \times \frac{1}{\mu}\mu_0 H_s \tag{1}$$

where A_s represents the impressed magnetic vector potential as a result of current source J_s, and A_r represents the reduced magnetic vector potential in the eddy current region. σ is the electrical conductivity, and μ is the permeability. In equation 1, H_s is the magnetic field generated by an excitation coil, which can be directly computed from any point P in free space from J_s:

$$H_s = \int_{\Omega_n} \frac{J_s(Q) \times r_{QP}}{4\pi \mid r_{QP} \mid^3} d\Omega_Q \tag{2}$$

where r_{QP} is the vector pointing from the source point Q to the field point P.
The impressed magnetic vector potential A_s can be written as:

$$\nabla \times A_s = \mu_0 H_s \tag{3}$$

Therefore, from equation 2 and equation 3, A_s is :

$$A_s = A_s = \int_{\Omega_n} \frac{\mu_0 J_s(Q)}{4\pi \mid r_{QP} \mid^2} d\Omega_Q \tag{4}$$

In MIT, the inductive coils are considered magneto-static not antennas; as such, the wave propagation effect can be ignored. Edge FEM is a useful technique to solve such problems by approximating the system as a combination of linear equations in small elements with appropriate boundary conditions. In edge FEM on a tetrahedral mesh, a vector field is represented using a basis vector function N_{ij} associated with the edge between nodes i and j:

$$N_{ij} = L_i \nabla L_j - L_j \nabla L_i \tag{5}$$

where L_i is a nodal shape function. Applying the edge element basis function to Galerkin's approximation [33, 34], one can obtain:

$$\int_{\Omega_e}(\nabla \times N \cdot \frac{1}{\mu}\nabla \times A_r)dv + \int_{\Omega_e} j\omega\sigma N \cdot A_r dv = \int_{\Omega_c}(\nabla \times N \cdot H_s)dv - \int_{\Omega_c}(N \cdot j\omega\sigma A_s)dv - \int_{\Omega_c}(\frac{1}{\mu}\mu_0\nabla \times N \cdot H_s)dv \quad (6)$$

where N is any linear combination of edge basis functions, Ω_e is the eddy current region, and Ω_c is the coil region. It can be seen from equation 6 that the right hand side can be solved with equations 2 and 4. The only unknown variable is the reduced vector potential A_r. By applying edge FEM, the second order partial differential equations can be computed by a combination of system linear equations, which can then be processed through Matlab. The A_r can be obtained using the biconjugate gradients stabilized method to solve the system linear equation [35]:

$$SA_r = b \quad (7)$$

where $S = S_r + jS_i$, which is a complex matrix; b is the right hand side current density, which is also complex. By solving the reduced magnetic vector potential A_r, one is able to evaluate the induced voltages in the measuring coils. The induced voltages can be calculated using a volume integration form:

$$V_{mn} = -j\omega \int_{\Omega_c} A \cdot J_0 dv \quad (8)$$

where $A = A_s + A_r$, and J_0 is a unit current density passing through the coil.
The sensitivity matrix is essential in MIT as it realises the linearisation between the conductivity and the induced voltages. The elements of the Jacobian matrix can be expressed according to [36, 37]:

$$\frac{\partial V_{mn}}{\partial \sigma_k} = -\omega^2 \frac{\int_{\Omega_k} A_m \cdot A_n dv}{I_0} \quad (9)$$

where V_{mn} is the measured voltage, σ_k is the conductivity of voxel k, Ω_k is the volume of the perturbation (voxel k), A_m and A_n are, respectively, solutions of the forward solver when the excitation coil (m) is excited by I_0 and the sensing coil (n) is excited with unit current.
The MIT inverse problem computes the distribution of the conductivity through measured voltages, which usually makes use of the forward model as part of the solving process. In this paper, newton one step error reconstruction (NOSER) is used to reconstruct images [38]. The reconstruction relies on the fact that for small changes, the measurements can be approximated in a linear fashion with the regularisation parameters:

$$x = (J^T J + \alpha R)^{-1} J^T b \quad (10)$$

where b is a column vector consisting M induced voltages (measurements), and x is a column vector representing K voxels. J is a $M \times K$ matrix of the sensitivity map, which is calculated from the forward model, R is the diagonal element of $J^T J$, and α is a regularization parameter.

System analysis

This MIT system was initially developed for imaging materials with high electrical conductivity, such as metal. There are 153 unique coil pairs: 1-2, 1-3, ..., 1-18, 2-3, 2-4, ..., 17-18, resulting in a total of 153 independent measurements. The image reconstruction module extracts these measurements, performs the reconstruction algorithms, displays and updates the images. The signal to noise ratio (SNR) is taken to indicate the signal level of the system to the background noise level, which can be defined using an amplitude ratio as [39]:

$$SNR = 20log_{10}\frac{U_S}{U_N} \tag{11}$$

where U_S is the mean signal amplitude and U_N is the standard deviation of the measured signal amplitude. Due to the geometry of this system, the system SNR also depends on the separation of the two planar arrays. Figure 3 shows the first cycle of SNR measurements when two planar arrays are separated at $2, 4, 6, 8$ and $10cm$ respectively.

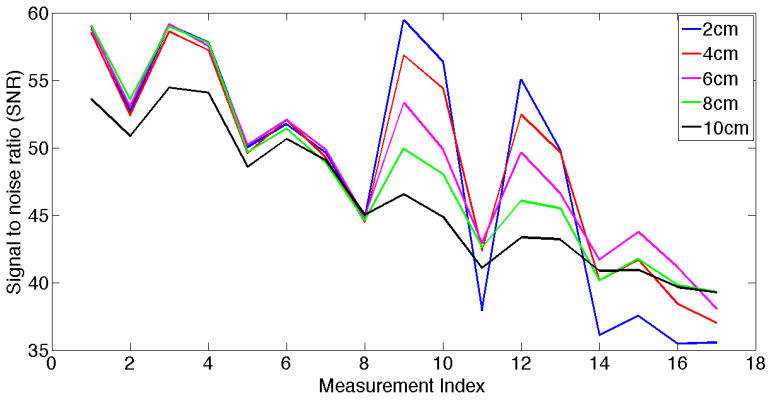

Figure 3. Signal to noise ratio for the first cycle of measurements against the separation of dual planes at $2, 4, 6, 8$ and $10cm$ respectively.

Several measurements are defined to analyse the system detectability, namely the neighbouring, opposite and diagonal measurement. The neighbouring measurement is used to describe the induced voltage measured from a pair of neighbouring coils that are in the same planar array (Figure 2b coil pair $1-2$ and coil pair $1-4$). The induced voltage measured from the coils directly facing each other is called the opposite measurement (coil pair $1-10$). The diagonal measurement refers to the induced voltage measured from any pair of coils that are located diagonally. This can be coil pairs either from the same planar array (Figure 2b coil pair $1-6$) or different planes (coil pair $3-16$). In this MIT study, the sensitivity maps demonstrate the relationship between the change in electrical properties and the voxel perturbation for a selected excitation/detection coil pair. It provides a visual approach to evaluate the system detectability in addition to the system SNR [36, 40, 41]. From a numerical point of view, the sensitivity map can be represented in a matrix form, which is also called the Jacobian matrix (equation 9).

Both front and side views of the sensitivity map for selected measurement pairs are shown in Figure 4, where Figure 4a shows the sensitivity contour for a neighbouring measurement, Figure 4b shows the sensitivity contour for an opposite measurement, and Figure 4c and 4d show the sensitivity contours for two diagonal measurements. In all cases, the sensitivity maps shown below are calculated for the free space scenario, i.e. there is no conductive materials presented in between.

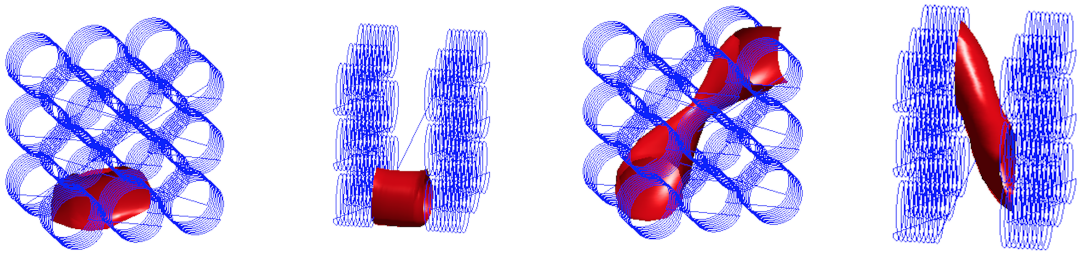

front view (a) side view (b) front view (c) side view (d)

Figure 4. Sensitivity maps for (a) a neighbouring measurement from coil 1 and 2; (b) an opposite measurement from coil 1 and 10; (c) a diagonal measurement from coil 1 and 9; (d) a diagonal measurement from coil 1 and 18.

The neighbouring measurement has a higher SNR due to a closer distance between a neighbouring coil pair. The opposite measurements capture the material property change from a different plane. Compared to the neighbouring and opposite measurements, the diagonal measurements have relatively lower induced voltages and as such, result in lower SNR. However, the diagonal measurements contribute to the depth detection, which is an important parameter to characterise the properties underneath the surface. The higher SNR usually comes from the coils in the same plane (Figure 3), providing that the distance between neighbouring coils is smaller than the distance between opposite coils; as is the case in this study. This can be illustrated in Figure 5, showing the included voltages from two planes $4cm$ apart. Taking the first cycle as an example, the strongest signal is due to the two neighbouring measurements − measurements 1 and 3, where the induced voltages of both are approximately $0.5V$ − and the highest measured voltage is induced between an opposite measurement − measurement 9, where the induced voltage is just over $0.1V$ − is almost 5 times lower than measurement 1.

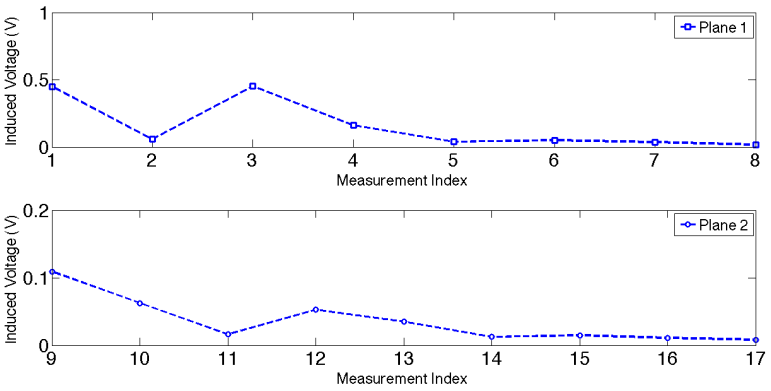

Figure 5. The first cycle of measurements for two plane of coils when coil 1 is used as an excitation coil, and the remaining used as receivers.

To allow the signal to penetrate the material under testing, an appropriate operating frequency and separation between two planes of planar coils are required. It was pointed out in [29] that for a single planar MIT system with a similar experimental setup, one can expect a maximum of $3-4cm$ of depth detection underneath the array. The driving frequency is an important factor in a MIT system. Lower frequency measurements penetrate the surface of the material and high frequency measurements thread around the surface of the material. In order to determine the suitable driving frequency, one needs to take the skin depth into consideration. In the quasi-steady electromagnetic field, the skin effect depth of general CFRP can be approximated by equation 12 [42]. As CFRP composites are nonmagnetic materials, the relative magnetic permeability of the CFRP is set to 1.

$$\delta = \sqrt{\frac{2}{\pi f \sigma \mu_0}} \tag{12}$$

where f is the driving frequency, σ is the electrical conductivity, and μ_0 is the unity permeability . In the frequency order of $10^4 Hz$, the skin depth of widely used CFRP is between $50-100mm$ [42]. For the normal conductance of a metallic material, the electrical conductivity is higher than that of CFRP, which means that for the same given frequency, the skin depth of CFRP is larger than the eddy current penetration for metal. For a MIT system designed for metal detection, the driving frequency is usually around $5-100KHz$ [43]. This is a suitable operational range for the damage identification of composite material, in fact, if the system hardware allows, the driving frequency can be increased to the MHz range in an attempt to increase the system SNR. In the lower MHz frequency range, laminated CFRP composites can be assumed to be a homogeneous conductive material [44], and as such, it is feasible to use this dual plane MIT system for this application. Based on the nature of our in-house low frequency MIT system, design specification of the dual planar arrays, the SNR analysis, and the properties of the CFRP samples used in this study, a separation of $4cm$ between two planes and an operational frequency of $50KHz$ are determined for experimental evaluation.

Three metallic cubes are used in the following experiments to test the stability and detectability of the this system (Figure 2a). Figure 6 shows the detection of two

metallic cubes in three different locations in relation to each other. The dimensions of the cubes are $1.4 \times 1.4 \times 1.2 cm^3$ and $1.2 \times 1.2 \times 1.4 cm^3$ respectively. Both sliced images and 3D contour images are shown in the top and bottom rows of Figure 6. For the 3D contour images, the dual planar coils are simulated in addition to the reconstructed inclusion to demonstrate the positions of the inclusion in relation to the coils in free space. The same visualisation approach is used for the remaining experimental results in this section.

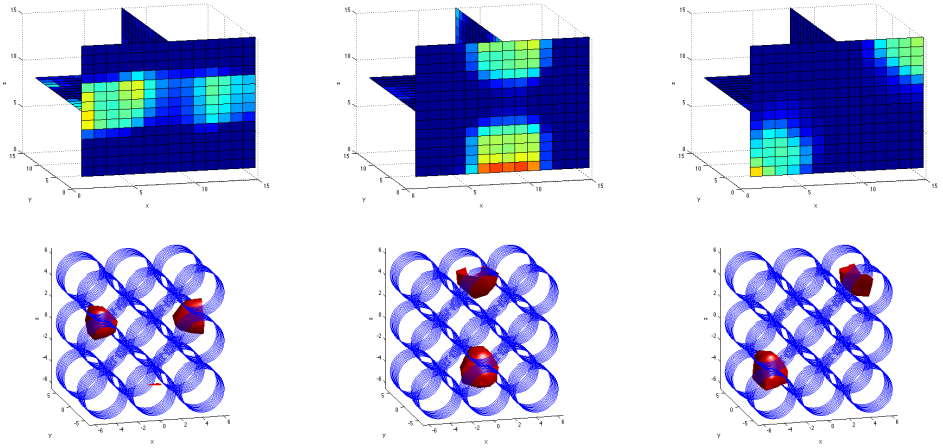

(a) (b) (c)

Figure 6. Detection of two steel samples in different locations.

Figure 7 shows the experimental results of an individual sample under testing. The dimension of the cube used for this experimental setup is $1.2 \times 1.2 \times 1 cm^3$. In all cases, the samples are placed between two planar coils. The samples have a conductivity of $1.45 \times 10^6 s/m$ and a relative permeability of 4000.

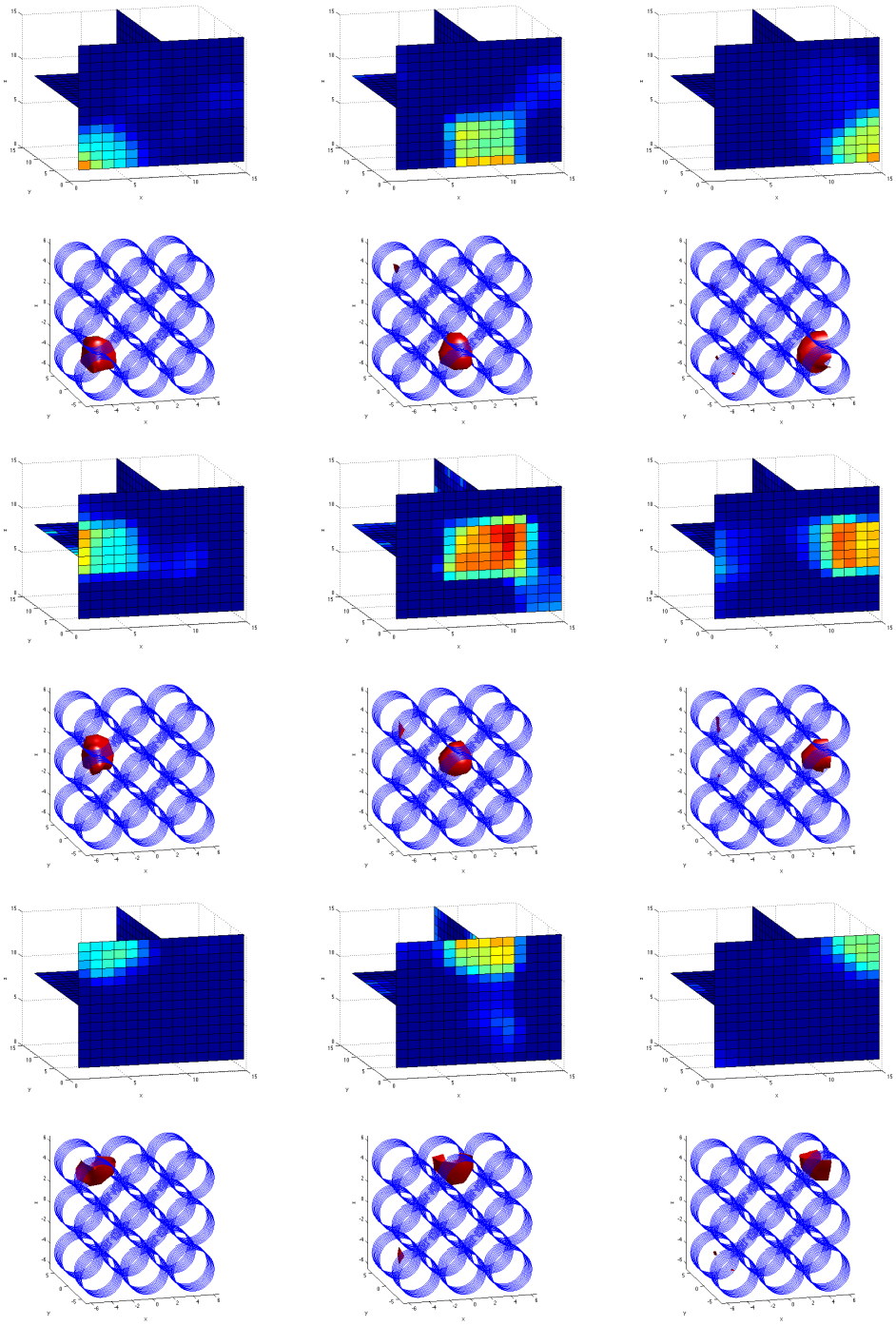

Figure 7. Detection of an individual steel sample in different locations.

Inspection of hidden damages in CFRP

The CFRP samples used in this study are made of HexPly M21 epoxy matrix, which is a high performance, toughened epoxy resin system supplied in primary aerospace structures. The physical properties of the epoxy matrix are listed in Table 1. The hidden damages are created using polytetrafluoroethylene (PTFE) rings and embedded in the $10mm$ thickness samples. The core is comprised of 35 layers of laminates CFRP , and is surrounded at each side by a further 10 layers of the same. An additional 10 layers are used to expand the sample to its final dimension of $10mm$. Finally, a peel ply finish is applied to each side. The schematic representation of the CFRP samples are shown in Figure 8, where 8a shows a CFRP sample with one hidden defect in the centre, and 8b shows a CFRP sample with four hidden defects.

Fibre Mass (g/m^2)	194
Nominal Prepreg Mass (g/m^2)	294
Theoretical Calculated Cured Ply Thickness (mm)	0.184
Theoretical Calculated Fibre Volume (%)	59.2
Resin Density (g/cm^3)	1.28
Fibre Density (g/cm^3)	1.78
Theoretical Calculated Laminate Density (g/cm^3)	1.58

Table 1. Physical properties of the HexPly M21 epoxy matrix.

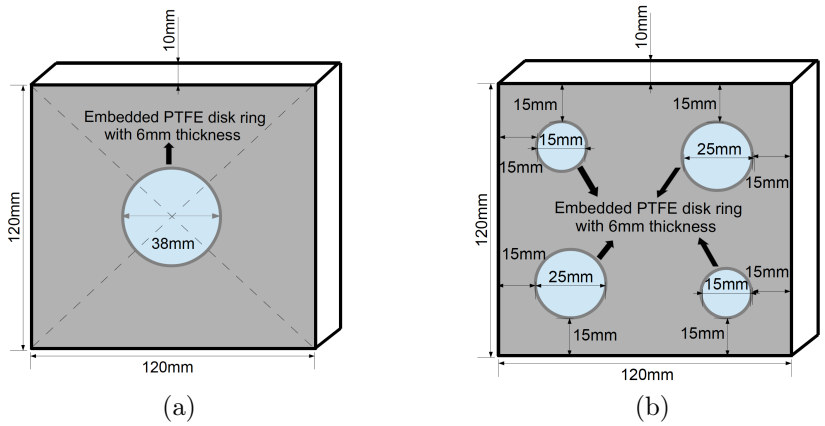

(a) (b)

Figure 8. CFRP samples with: (a) one hidden defect in the centre; (b) four hidden defects.

The reconstructed images for both CFRP samples are shown using sliced image and 3D contour images (Figure 9). The background measurement is taken from an undamaged CFRP sample with the same dimensions. This is the first step of calibrating in the input measurements in the inverse solver. The damages occur on the subsurface within the laminate architecture of the composite, which makes them barely visible to inspectors. Therefore, in both Figure 9a and 9d, an approximation of the defected areas are marked in dashed line. In Figure 9b and 9e, the colour blue represent the CFRP samples with all other colours representing the damaged areas.

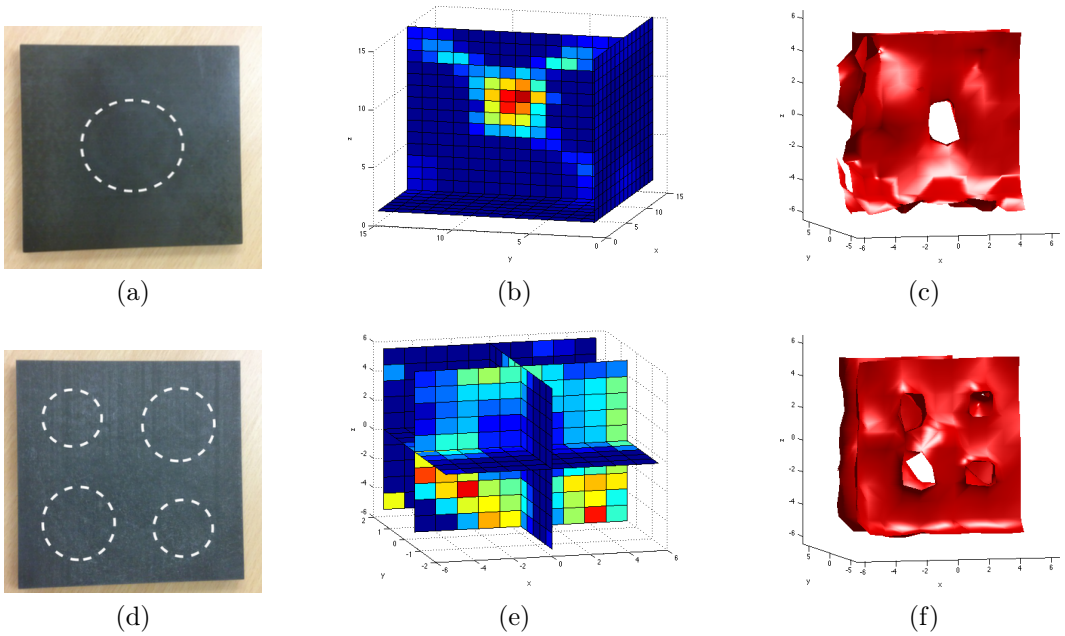

Figure 9. (a) True CFRP sample with one defect; (b) Reconstructed image of (a) using slice visualisation; (c) 3D contour visualisation of (a); (d) True CFRP sample with four defects; (e) reconstructed image of (d) using slice visualisation; (f) 3D contour visualisation of (d).

For 3D contour images in Figure 9c and 9f, the highlighted red areas are the CFRP samples.

Conclusions

A dual plane MIT system is proposed for the identification of hidden defects in CFRP. The MIT system used in this study was initially tested using metallic samples. The fundamental physics and the mathematical solving process of MIT are studied to extend this technique in the area of CFRP inspection. The system stability and detectability is analysed through both simulation and experiments. The experimental results show that different sizes and locations of hidden damage can be identified using the proposed MIT system with the given sensor geometry and experimental setup. Due to the low resolution of this technique, the size differences of the defects cannot be distinguished at this stage of the research. Nevertheless two samples are not sufficiently representative to cover all possible manufacturing defects or impact damage which may occur in real industrial environment. For examples, the impact damage could result in an altered electrical conductivity, which might not be as high contrast as the conductivity changes shown in this work. This study represents the proof of principles for MIT as a viable means to be developed as an in-service SHM technique for CFRP. Further development in this application are needed, including the study of MIT sensor array topology, the development of multifrequency excitation, the design of a rapid data handling unit and computational modeling of the forward and inverse problems for anisotropic eddy currents. These will be subjects of our follow

up studies.

Acknowledgments

The authors would like to thank the composites research unit in Department of Mechanical Engineering at University of Bath for manufacturing the CFRP samples used in this study and the Schlumberger Foundation Faculty for the Future for research funding.

References

[1] R. D. Adams and P. Cawley, "A review of defect types and nondestructive testing techniques for composites and bonded joints," *NDT International*, vol. 21, no. 4, pp. 208–222, 1988.

[2] C. C. H. Guyotta, P. Cawleya, and R. D. Adamsb, "The non-destructive testing of adhesively bonded structure: a review," *The Journal of Adhesion*, vol. 20, no. 2, pp. 129–159, 1986.

[3] D. E. W. Stone and B. Clarke, "Ultrasonic attenuation as a measure of void content in carbon-fibre reinforced plastics," *Non-Destructive Testing*, vol. 8, pp. 137–145, 1975.

[4] J. L. Rose, M. J. Avioli, and R. Bilgram, "A feasibility study on the nondestructive evaluation of an adhesively bonded metal to metal bond: an ultrasonic pulse echo approach," *British journal of non-destructive testing*, vol. 25, pp. 67–71, 1983.

[5] S. Yashiro, J. Takatsubo, N. Toyama, T. Okabe, and N. Takeda, "Delamination detection in holed cfrp laminates using visualized ultrasound propagation," *Transactions of the Japan Society of Mechanical Engineers Series A*, vol. 72, no. 12, pp. 1882–1887, 2006.

[6] A. Diaz, M. Guizar-Sicairos, A. Poeppel, A. Menzel, and O. Bunk, "Characterization of carbon fibers using x-ray phase nanotomography," *Carbon*, vol. Article in press, 2013.

[7] D. J. Bull, S. M. Spearing, I. Sinclair, and L. Helfen, "Three-dimensional assessment of low velocity impact damage in particle toughened composite laminates using micro-focus x-ray computed tomography and synchrotron radiation laminography," *Composites Part A: Applied Science and Manufacturing*, vol. 52, no. 0, pp. 62 – 69, 2013.

[8] U. Hassler, M. Rehak, and R. Hanke, "Carbon fibre preform inspection by circular x-ray tomosynthesis," pp. 590–592, 2008.

[9] S. A. Grammatikos, E. Z. Kordatos, T. E. Matikas, C. David, and A. S. Paipetis, "Current injection phase thermography for low-velocity impact damage identification in composite laminates," *Materials and Design*, vol. 55, pp. 429–441, 2014.

[10] G. Zauner, G. Mayr, and G. Hendorfer, "Comparative defect evaluation of aircraft components by active thermography," vol. 7251, 2009.

[11] M. P. D. Goeje and K. E. D. Wapenaar, "Non-destructive inspection of carbon fibre-reinforced plastics using eddy current methods," *Composites*, vol. 23, no. 3, pp. 147 – 157, 1992.

[12] H. Heuer, M. H. Schulze, and N. Meyendorf, "High resolution inspection of carbon fiber materials by eddy current techniques," *2nd International Symposium on NDT in aerospace*, vol. Mo.2.A.3, 2010.

[13] M. H. Schulze, H. H. Heuer, M. Kuttner, and N. Meyendorf, "High-resolution eddy current sensor system for quality assessment of carbon fiber materials," *Microsystem Technologies*, vol. 16, no. 5, pp. 791–797, 2010.

[14] K. Koyama, H. Hoshikawa, and G. Kojima, "Eddy current nondestructive testing for carbon fiber-reinforced composites," *Journal of Pressure Vessel Technology, Transactions of the ASME*, vol. 135, no. 4, 2013.

[15] A. Baltopoulos, N. Polydorides, L. Pambaguian, A. Vavouliotis, and V. Kostopoulos, "Damage identification in carbon fiber reinforced polymer plates using electrical resistance tomography mapping," *Jounal of composites materials*, vol. 47, no. 26, pp. 3285–3301, 2012.

[16] B. R. Loyola, T. M. Briggs, L. Arronche, K. J. Loh, V. L. Saponara, G. O'Bryan, and J. L. Skinner, "Detection of spatially distributed damage in fiber-reinforced polymer composites," *Structural Health Monitoring*, vol. 12, no. 3, pp. 225–239, 2013.

[17] R. Schueler, S. P. Joshi, and K. Schulte, "Damage detection in cfrp by electrical conductivity mapping," *Composites science and technology*, vol. 61, pp. 921–930, 2001.

[18] A. Renner, W.-J. Fischer, and U. Marschner, "A new imaging approach for in-situ and ex-situ inspections of conductive fiber reinforced composites by magnetic induction tomography (mit)," *Journal of Intelligent Material Systems and Structures*, pp. 897–902, 2012.

[19] R. Casanas, H. Scharfetter, A. Altes, A. Remacha, P. Sarda, J. Sierra, R. Merwa, K. Hollaus, and J. Rosell, "Measurement of liver iron overload by magnetic induction using a planar gradiometer: preliminary human results," *Physiological measurement*, vol. 25, no. 1, p. 315, 2004.

[20] A. Korjenevsky, V. Cherepenin, and S. Sapetsky, "Magnetic induction tomography: experimental realization," *Physiological Measurement*, vol. 21, no. 1, p. 89, 2000.

[21] X. Ma, A. J. Peyton, S. R. Higson, and P. Drake, "Development of multiple frequency electromagnetic induction systems for steel flow visualization," *Measurement Science and Technology*, vol. 19(094008), 2008.

[22] H. Scharfetter, R. Casanas, and J. Rosell, "Biological tissue characterization by magnetic induction spectroscopy (mis): requirements and limitations," *IEEE Transactions on Biomedical Engineering*, vol. 50, no. 7, pp. 870–880, 2003.

[23] H. Griffiths, W. R. Stewart, and W. Gough, "Magnetic induction tomography: A measuring system for biological tissues," *Annals of the New York Academy of Sciences*, vol. 873, pp. 335–345, 1999.

[24] H. Y. Wei and M. Soleimani, "A magnetic induction tomography system for prospective industrial processing applications," *Chinese Journal of Chemical Engineering*, vol. 20, no. 2, pp. 406–410, 2012.

[25] L. Janousek, "Influence of selected parameters on eddy currents attenuation in non-destructive inspection," *Komunikacie*, vol. 15, no. 2A, pp. 102–106, 2013.

[26] H. Y. Wei and M. Soleimani, "Theoretical and experimental evaluation of rotational magnetic induction tomography," *IEEE on Instrumentation and Measurement*, vol. pp, pp. 1–8, 2012.

[27] H. Y. Wei, L. Ma, and M. Soleimani, "Volumetric magnetic induction tomography," *Measurement Science and Technology*, vol. 23, no. 5, p. 055401, 2012.

[28] L. Ma and M. Soleimani, "Limited angle and limited data electromagnetic induction tomography: experimental evaluation of the effect of missing data," *Measurement Science and Technology*, vol. 23, no. 12, p. 125406, 2012.

[29] L. Ma, H.-Y. Wei, and M. Soleimani, "Planar magnetic induction tomography for 3d near subsurface imaging," *Progress In Electromagnetics Research*, vol. 138, pp. 65–82, 2013.

[30] L. Ma, H. Y. Wei, and M. Soleimani, "Pipeline inspection using magnetic induction tomography based on a narrowband pass filtering method," *Progress In Electromagnetics Research M*, vol. 23, pp. 65–78, 2012.

[31] O. Biro, "Edge element formulations of eddy current problems," *Computer Methods in Applied Mechanics and Engineering*, vol. 169, pp. 391–405, 1999.

[32] O. Biro and K. Preis, "An edge finite element eddy current formulation using a reduced magnetic and a current vector potential," *IEEE Transactions on Magnetics*, vol. 36, no. 5, pp. 3128–3130, 2000.

[33] N. A. Golias, C. S. Antonopoulos, T. D. Tsiboukis, and E. E. Kriezis, "3d eddy current computation with edge elements in terms of the electric intensity," *The International Journal for Computation and Mathematics in Electrical and Electronic Engineering*, vol. 17, no. 5/6, pp. 667–673, 1998.

[34] D. C. Barber and B. H. Brown, "Applied potential tomography," *Journal of Physics E: Scientific Instruments*, vol. 17, no. 9, pp. 723–734, 1984.

[35] M. Soleimani and W. R. B. Lionheart, "Absolute conductivity reconstruction in magnetic induction tomography using a nonlinear method," *IEEE Transactions on Medical Imaging*, vol. 25, no. 12, pp. 1521–1530, 2006.

[36] D. N. Dyck, D. A. Lowther, and E. M. Freeman, "A method of computing the sensitivity of the electromagnetic quantities to changes in the material and sources," *IEEE Transactions on Magnetics*, vol. 30, pp. 3415–3418, 1994.

[37] M. Soleimani and W. R. B. Lionheart, "Image reconstruction in three-dimensional magnetostatic permeability tomography," *IEEE Transactions on Magnetics*, vol. 41, pp. 1274–1279, 2005.

[38] M. Cheney, D. Isaacson, J. C. Newell, S. Simske, and J. Goble, "Noser: An algorithm for solving the inverse conductivity problem," *International Journal of Imaging Systems and Technology*, vol. 2, no. 2, 1990.

[39] R. Merwa and H. Scharfetter, "Magnetic-induction-tomography: evaluation of the point-spread-function and analysis of resolution and image distortion," *Physiological measurement*, vol. 28, pp. 313–324, 2007.

[40] A. J. Peyton, Z. Z. Yu, G. Lyon, S. Al-Zeibak, J. Ferreira, J. Velez, F. Linhares, A. R. Borges, H. L. Xiong, N. H. Saunders, and M. S. Beck, "An overview of electromagnetic induction tomography: description of three different systems," *Measurement Science and Technology*, vol. 7, pp. 261–271, 1996.

[41] S. Ramli and A. J. Peyton, "Feasibility study of planar-array electromagnetic inductance tomography (emt)," in *1st World Congress on Industrial Process Tomography, Buxton, Greater Manchester*, 1st World Congress on Industrial Process Tomography, Buxton, Greater Manchester, April 14-17 1999.

[42] A. Todoroki, "Skin effect of alternating electric current on laminated cfrp," *Advanced Composite Materials*, vol. 21, no. 5-6, pp. 477–489, 2012.

[43] H. Griffiths, "Magnetic induction tomography," *Measurement Science and Technology*, vol. 12, pp. 1126–1131, 2001.

[44] T. A. Ezquerra, M. T. Connor, S. Roy, M. Kulescza, J. Fernandes-Nascimento, and F. J. Balta-Calleja, "Alternating-current electrical properties of graphite, carbon-black and carbon-fiber polymeric composites.," *Composites Science and Technology*, vol. 61, pp. 903–909, 2001.